IEEE Photonics Journal
An IEEE Photonics Society Publication

Design of a 250-Gbit/s SiGe HBT Electrooptic Modulator

Volume 3, Number 5, October 2011

Tuhin Guha Neogi, Student Member, IEEE
Guofu Niu, Senior Member, IEEE
Daniel Connelly
John D. Cressler, Fellow, IEEE
Zhaoran Rena Huang, Senior Member, IEEE
John F. McDonald, Life Senior Member, IEEE

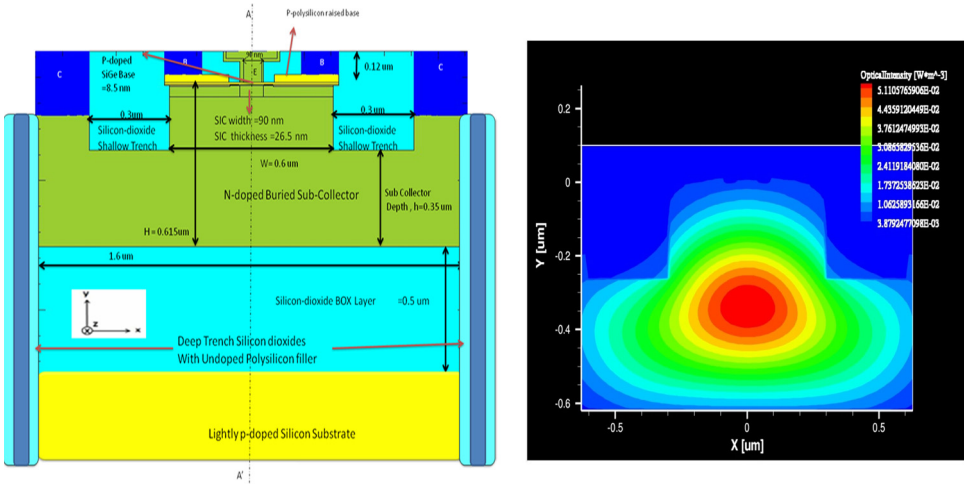

DOI: 10.1109/JPHOT.2011.2169658
1943-0655/$26.00 ©2011 IEEE

IEEE photonics SOCIETY

IEEE

Design of a 250-Gbit/s SiGe HBT Electrooptic Modulator

Tuhin Guha Neogi,[1] *Student Member, IEEE*, Guofu Niu,[2] *Senior Member, IEEE*, Daniel Connelly,[4] John D. Cressler,[3] *Fellow, IEEE*, Zhaoran Rena Huang,[1] *Senior Member, IEEE*, and John F. McDonald,[1] *Life Senior Member, IEEE*

[1]Electrical, Computer, and Systems Engineering Department, Rensselaer Polytechnic Institute, Troy, NY 12180 USA
[2]Alabama Microelectronics Science and Technology Center, Electrical and Computer Engineering Department, Auburn University, Auburn, AL 36849 USA
[3]School of Electrical and Computer Engineering, Georgia Institute of Technology, Atlanta, GA 30332-0250 USA
[4]Synopsys Inc., Dallas, TX 75254 USA

DOI: 10.1109/JPHOT.2011.2169658

Manuscript received August 12, 2011; revised September 14, 2011; accepted September 16, 2011. Date of publication September 26, 2011; date of current version October 11, 2011. Corresponding author: T. Guha Neogi (e-mail: guhant@rpi.edu).

Abstract: We present a rigorous electrical and optical analysis of a highly scaled, graded-base, SiGe heterojunction bipolar transistor (HBT) electrooptic (EO) modulator. In this study, we propose a 2-D electrical model and a 3-D optical model for a graded-base SiGe HBT structure that is capable of operating at a data bit rate of 250 Gbit/s or higher. In this structure, apart from a polysilicon/low doped emitter (width = 90 nm) and a strained SiGe graded base (depth = 8.5 nm), a selectively implanted collector (SIC) (depth = 26 nm) is introduced. Furthermore, at a base-emitter swing of 0 to 1.0 V, this model predicts a rise time of 3.48 ps and a fall time of 0.55 ps. Optical simulations predict a π phase shift length (L_π) of 204 μm, with an extinction ratio of 13.2 dB at a wavelength of 1.55 μm.

Index Terms: Semiconductor device modeling, integrated optics, optical modulation, plasma dispersion effect, SiGe, heterojunction bipolar transistors.

1. Introduction

As interconnect bandwidth requirements scale to 10 Tb/s and beyond, higher levels of integration will be required to increase bandwidth per pin (or optical connector) at significantly reduced cost. Over the last decade, remarkable progress has been made in research on silicon photonic devices for interconnect applications. The use of silicon as a material for these photonic applications promises high-volume manufacturing using complementary metal–oxide–semiconductor (CMOS)-compatible processes. In 2007, IBM reported a P-I-N silicon modulator with bit rates of 10 Gbit/s and an L_π of 100 to 200 μm [1]. In the same year, Intel demonstrated a PN junction based high-speed modulator of 40 Gbit/s with an L_π of 1 mm in a Mach–Zehnder Interferometer (MZI) configuration using a carrier depletion structure combined with travelling wave electrodes (TWEs) [2]. In 2005, a depletion mode PN junction based SOI modulator was reported with rise and fall times of 7 ps with an effective bandwidth of 60 GHz [3]. In 2011, a hybrid silicon travelling-wave electroabsorption modulator has been demonstrated at 50 Gbit/s [4]. Recently, IBM demonstrated a 30-Gbit/s silicon micro-ring modulator operating at a low power of 335 fJ/bit [5]. The use of SiGe-on-Si technology for high-speed optical modulation based on a free carrier plasma effect dates back to Soref's work in

1990 [6]. Several of these papers provide experimental verification that the free carrier effect can be utilized for electrooptic (EO) modulation. The question that remains, however, is how fast this effect can operate and with what physical length, propagation loss, and energy per bit.

Our previous work on a SiGe heterojunction bipolar transistor (HBT) EO modulator reported a simulated operation bandwidth limited to 80 Gbit/s at an active length of 240 μm [7] with a model that approximated a 130-nm minimum feature size device in actual commercial production today. One motivation for exploring the SiGe HBT is that these devices are often required for the serializer/deserializer (SERDES) support circuitry at high bit rates. In the present paper, we examine a theoretical aggressively scaled SiGe HBT that may approximate a device that is two device generations more advanced than available today. In this new structure, which we explore here in depth, MEDICI [8] is used for analysis of 2-D electrical transient simulations and Synopsis' Sentaurus [9] for 3-D electrical and optical DC simulations. We designed an aggressively scaled SiGe HBT structure of our previous model [7] to explore the maximum bandwidth achievable operating this device as an EO modulator. The key contribution of this study is the improvement in the rise and fall times of the EO modulator during large signal switching. This is achieved by the introduction of an ultrathin and compressively strained SiGe epitaxial base on the selectively implanted collector (SIC). The compressive strain in the SiGe base enhances the lateral and vertical hole mobility. The presence of gradient germanium mole fraction in the vertical base results in the acceleration of minority carrier electrons in base.

In this paper, we organize our study in the following manner. We propose the aggressively scaled SiGe HBT structure based on a proposed 2-D SiGe HBT design optimized for electrical performance [10]. We also discuss further modifications made to this device to use it as a highly efficient and fast optical modulator. For any bipolar transistor, it is imperative to study and extract the electrical DC, AC characteristics and the bias conditions for its required operation regime. Hence, we analyze the terminal characteristics of the SiGe HBT, namely, small-signal cutoff frequency, current gain, and Gummel characteristics. We present a comparative study of the electrical behavior of the device at different doping and graded Germanium profiles. At the same time, we adhere to the high-volume manufacturing feasibility of this device using existing SiGe BiCMOS processes. After determining the optimum electrical bias conditions required for the high-speed operation, we study the transient terminal currents and electron hole density distributions in this structure. Finally, a comparative discussion on the active length of the modulator (L_π), dynamic power consumed, propagation loss, and extinction ratio of the optical mode is presented. Apart from speed and efficiency, the key advantage in opting for a modulator using the SiGe HBT technology is the implementation of the modulator driver circuits using the similar SiGe technology, as demonstrated in 2004 [11].

Additionally, at extremely thin base widths (below 10 $\sim$ 20 nm), the numerical simulation techniques used should accurately model the transport of highly energetic electrons and holes. We also discuss the physical models and parameters used for this heterojunction device in both the electrical and optical domains. Nanoscale dimensions in the collector leads to higher field, which is a concern for breakdown voltage, which we also simulate.

Taken together, these simulations strongly support the primary conclusion of this study that the proposed SiGe EO modulator should be capable of operating at 250 Gbit/s data rates or perhaps even beyond. To the best of our knowledge, such a device would be the fastest Si EO modulator ever proposed (and analyzed) which operates based on the free-carrier plasma effect.

2. Device Structure

The proposed 2-D SiGe HBT structure is shown in Fig. 1. The typical parameters that represent the SiGe HBT are the base thickness and the emitter width (W_E). In this design, a heavily n-doped polysilicon emitter with uniform doping concentration of 1×10^{21} cm^{-3}, emitter width of 90 nm, and thickness of 100 nm is chosen. There are two symmetric base contacts and two symmetric collector contacts on each side of the emitter. The base consists of p-doped strained SiGe alloy with a thickness of 8.5 nm and width of 0.6 μm. The graded germanium mole fraction plays an important

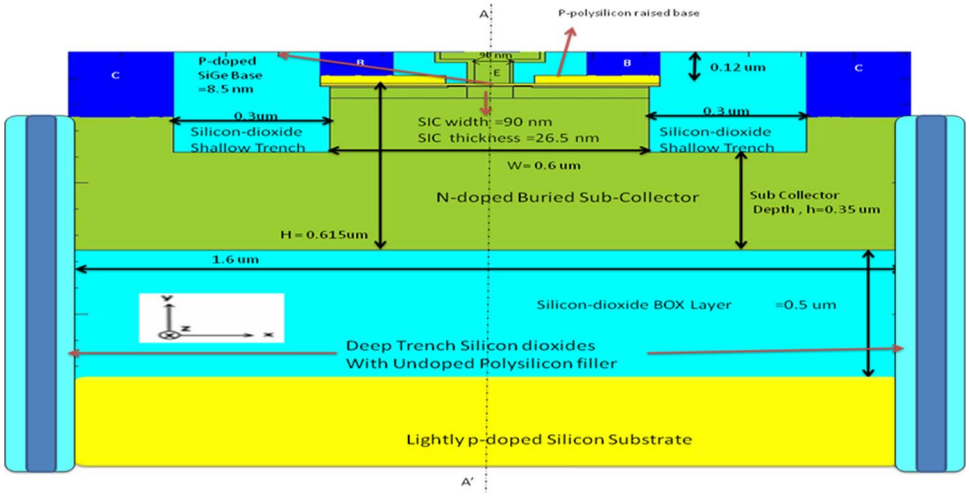

Fig. 1. Schematic cross-section of the proposed HBT EO modulator model.

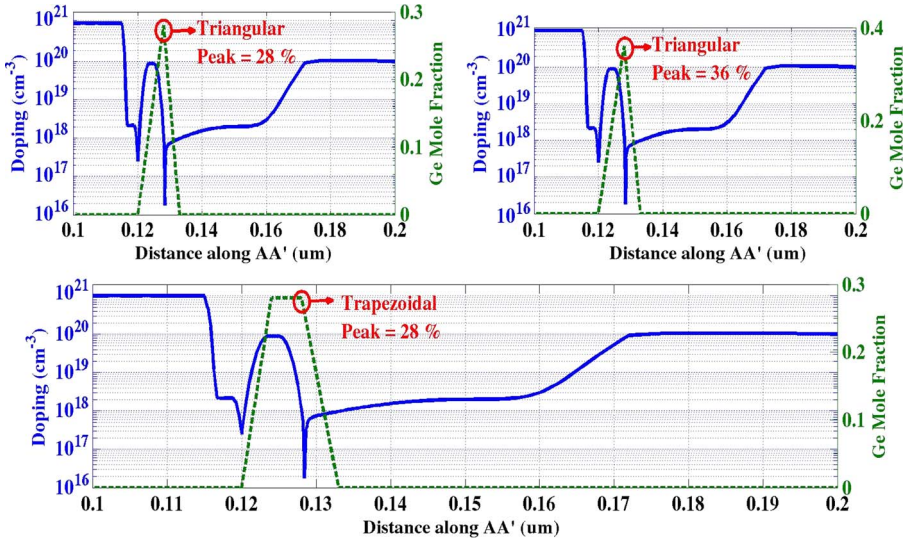

Fig. 2. Three similar doping profiles and three different Ge Mole Fractions verse the vertical distance at the device center (AA′) from the surface. Triangular Ge peak of 28% (top left), Triangular Ge peak of 36% (top right), and Trapezoidal Ge peak of 28% (bottom).

role in reducing the transit time of the electrons in the SiGe base and, hence, in improving the speed of the modulator. Hence, we study both the trapezoidal profile and triangular profile with different peak Ge fractions, as shown in Fig. 2. The thin epitaxial base has a peak doping of 8×10^{19} cm^{-3}. A highly doped p-polysilicon $(3 \times 10^{20}$ cm$^{-3})$ raised extrinsic base with a thickness of 30 nm is defined on each side of the narrow emitter. A narrow distance between the edge of emitter and the edge of raised extrinsic base is chosen to reduce the extrinsic base resistance. A SIC region with a thickness of 30 nm and width equal to that of the emitter (90 nm) is also incorporated. The peak doping level of 2×10^{18} cm^{-3} is chosen in the SIC with a downward gradient toward the base. As shown in Fig. 1, there are two shallow trenches (ST) of 0.25 μm thickness beside the base contacts. The distance between the two ST's are effectively chosen as 0.6 μm to fit the mode of the optical beam of wavelength $= 1.55$ μm in free space and $\sim$0.45 μm in silicon material. This also ensures single mode operation, as shall be seen in later sections. The two deep trenches are defined on

each side of the collector contacts. These trenches are filled with a thin 0.1 μm layer of silicon dioxide sidewalls and an undoped polysilicon filler to reduce stress. Silicon dioxide behaves as an electrical insulator and additionally confines the light due to its low refractive index compared with silicon. The remaining part of the low doped (N^-) collector region assumes the background doping of 1×10^{16} cm^{-3} on each side of SIC. The buried subcollector of width 1.6 μm, depth of 0.35 μm and high doping concentration of 1.0×10^{20} cm^{-3} is defined to reduce the resistance of the subcollector region which connects the intrinsic base–collector (BC) junction to the collector contact. The reach-through layer connecting the subcollector layer and the collector contacts assumes a high doping of 1×10^{20} cm^{-3}. The doping profile along the center of the device cross section (AA′) is plotted in Fig. 2. In later sections, we will discuss the impact of different subcollector doping levels on the speed and optical properties of the modulator. A buried oxide layer with a thickness of 0.5 μm and width of 1.6 μm is assumed just below the subcollector. Fig. 1 assumes a silicon substrate below the buried oxide with a p-doped concentration of 1×10^{16} cm^{-3}.

In the emitter design, a low doped emitter $(2.0 \times 10^{18}$ cm$^{-3})$ is included between the high doped emitter $(1.0 \times 10^{21}$ cm$^{-3})$ and the epitaxial SiGe base, as shown in Fig. 2. The purpose is to reduce tunneling current and generation/recombination (G/R) current. The reason for the reduction in tunneling current is that the doping concentration at the emitter–base (EB) junction is smaller when a low-doped emitter is used, which leads to a longer carrier lifetime and, hence, less of a G/R current. Another advantage is that the low-doped emitter is depleted, and the emitter-base space charge region (SCR) is located at this region. Therefore, base width modulation due to the change of V_{BE} is reduced [12]. In order to decrease the base transit time dramatically, the base thickness is scaled to as narrow as $8 \sim 9$ nm. To have a low base resistance and to replicate the profile after fabrication, a nonuniformly doped base profile is used, with the peak base doping as high as $(9.0 \times 10^{19}$ cm$^{-3})$. A 30-nm-thick moderately doped retrograde collector profile is used to reduce the collector transit time. Higher collector doping leads to lower collector transit time. However, as we will show in Section 4.1.3, breakdown voltage does not degrade too much at these nanoscale dimensions of the SiGe HBT thanks to nonequilibrium transport effects. We also report the DC safe operating area (SoA) bias conditions for this modulator.

3. Device Modeling

The transient, DC, and breakdown voltage of the SiGe HBT EO modulator are explored with a 2-D simulation tool: MEDICI. The key parameters examined include the free-carrier concentrations and distributions. These parameters give rise to optical field confinement, injection current, DC characteristics, and electrical power under transient conditions. A 3-D coupled electrical and optical simulator is used to design and analyze the mode confinement, π phase shift interaction length (L_π), transmission characteristics, modulation depth, and optical losses of the structure.

3.1. Electrical Model

With device scaling, not only the high electric field, but also the rapid changes of electric field over a short distance (field gradient) are present for scaled SiGe HBTs. As a result, the nonequilibrium carrier transport leads to high-order phenomena such as velocity overshoot. In order to model device functionality correctly, the energy balance (EB) equations are solved self-consistently together with Poisson's equation and electron and hole continuity equations. Therefore, the MEDICI simulations model the device parasitics implicitly. Due to the lack of experimental bandgap narrowing (BGN) data for SiGe, we assume here that the apparent BGN for SiGe is the same as for Si. Boltzmann statistics, as opposed to Fermi–Dirac statistics, are used in order to ensure physically consistent modeling of minority carrier concentration, as discussed in [13]. The Slotboom BGN model is used to model the heavy-doping induced BGN [10], [14]. The Philip's unified mobility model (PHUMOB) is used to be consistent with Slotboom's BGN model [13]. An electron relaxation time $\tau_n = 0.3$ ps is used based on calibration of simulation results against measured HBT characteristics [15]. Shockley–Read–Hall (SRH) recombination and Auger recombination models are used along with the other mentioned physical models. The 2-D simulation package MEDICI from

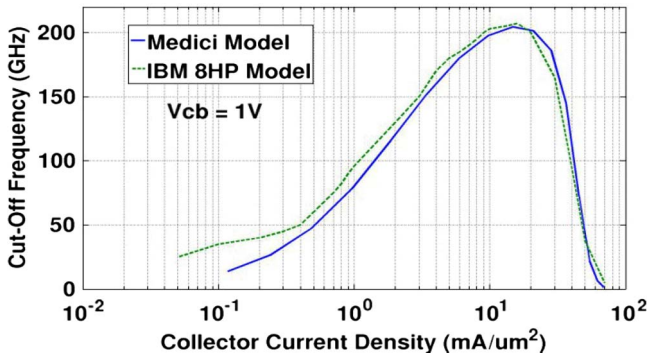

Fig. 3. SiGe HBT 8HP model from IBM compared to our SiGe HBT MEDICI model [7].

SYNOPSYS [8] is employed to analyze the electrical transient calculations of the proposed SiGe HBT. Suitability of this device modeling software to analyze electrical performance in SOI waveguides has been demonstrated by other authors [16], [17]. The accuracy of this device modeling software can be emphasized by the validation of IBM 8hp Model in our previous work [7], as shown in Fig. 3. This program simulates internal physics and device characteristics of semiconductor devices by solving Poisson's equation, the electron and hole continuity equations, as well as the EB equations numerically, which are necessary given the rapidly varying electric fields in this nanoscale structure. Ohmic contacts without additional contact resistance or capacitance have been assumed.

3.2. Optical Model

We use the bidirectional Beam Propagation method (BPM) [9] in 3-D for optical analysis of the wave propagation in the SiGe HBT waveguide. First, we recreate the SiGe HBT structure in Sentaurus with the exact dimensions, as shown in Fig. 1, and then replicate the doping profile, as shown in Fig. 2. Initially, the length of the structure is chosen to be 10 μm. This is used to reduce the computational time taken for electrical and optical simulation. Two separate DC electrical simulations are run (one under unbiased conditions and the other under biased conditions), as discussed in Section 4.2. From the values of the electron and hole carrier distributions in the SiGe HBT, the complex refractive index profile is generated as [18]

$$\Delta n = \Delta n_e + \Delta n_h = -\left[8.8 \times 10^{-22}\Delta N_e + 8.5 \times 10^{-18}(\Delta N_h)^{0.8}\right] \quad (1)$$

$$\Delta \alpha = \Delta \alpha_e + \Delta \alpha_h = [8.5 \times 10^{-18}\Delta N_e + 6.0 \times 10^{-18}\Delta N_h] \quad (2)$$

where Δn and $\Delta \alpha$ are the real part of refractive index and the absorption coefficient, respectively. In (1) and (2), ΔN represent the carrier density changes, with "e" and "h" denoting electron and hole densities, respectively. These equations show that the free carrier effect can be used to directly modulate phase or amplitude or both. The refractive index in silicon dioxide is assumed to be constant at 1.45. The use of crystalline Si (c-Si) instead of polysilicon or amorphous Si as the waveguide core reduces scattering and absorption losses [19]. Since the core of our waveguide lies in the SIC region, scattering losses due to surface roughness are negligible in SIC. However, the scattering losses due to the change in free carrier plasma are incorporated. The scattering losses in the polysilicon are higher, but low loss polysilicon with transmission loss of only 9 dB/cm at wavelength of $\lambda = 1.55$ μm has been demonstrated [20]. The transmission loss the highly doped polysilicon is assumed to be the sum of bulk loss (9 dB/cm) and the free carrier loss due to doping. The bidirectional simulator in Sentaurus also takes into account any backward reflections of the propagating wave. The fundamental mode of the waveguide is launched at $Z = 0$ μm and the output mode is extracted at $Z = 10$ μm. From the optical field data along Z direction the phase of the mode for unbiased and biased conditions are extracted. The difference in the phase between

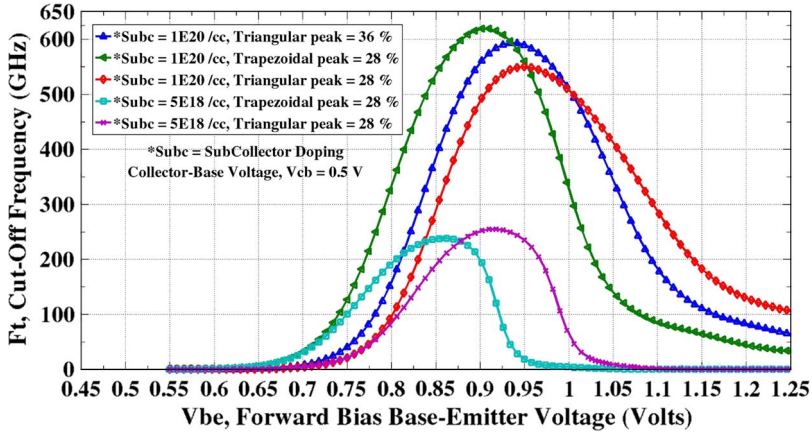

Fig. 4. Small-signal cutoff frequency of MEDICI model at various sub-collector doping and Ge graded profiles.

these two bias conditions at $Z = 10$ μm is used to compute the length required for π-phase shift (L_π). From the input mode Intensity and the output mode Intensity the propagation loss and extinction ratio are calculated.

4. Results and Discussion

4.1. Electrical Analysis

The small-signal cutoff frequency (f_T) of the modulator, the large-signal transient switching speed of the carriers, and the DC breakdown voltage was analyzed using our 2-D MEDICI model. The f_T analysis indicates the favorable bias conditions required to operate the modulator to achieve maximum speed and subsequently avoiding high-injection effects and excessive electrical stress. The breakdown voltage for the collector-base junction and the Gummel characteristics illustrate the SoA DC bias operation conditions and the acceptable collector voltages in particular.

4.1.1. Small-Signal Cutoff Frequency

The small-signal cutoff frequency (f_T) is extracted for different subcollector doping and Ge graded profiles, as shown in Fig. 4. At subcollector doping of 1.0×10^{20} cm^{-3} and 5.0×10^{18} cm^{-3}, the peak f_T is higher for a triangular profile than for a trapezoidal profile. Additionally, the peak f_T shifts to higher base-emitter input bias (V_{be}) levels. We will see later that the peak f_T frequency is not the correct representation of large-signal switching speed, but it gives an estimate of the operating input bias voltage, which is approximately $\sim$1 V in this case. At a lower subcollector doping of 5.0×10^{18} cm^{-3} the peak f_T drops significantly to 240–260 GHz because of the onset of high injection in the base-collector region at much lower voltages. Hence, it can be estimated that a triangular-shaped Ge graded profile with a subcollector doping of 1.0×10^{20} cm^{-3} are the best choice for designing a high-speed nanoscale dimension SiGe optical modulator.

4.1.2. Transient Switching Speed of the Carriers and Their Distributions

As shown in Fig. 5(a), an input voltage ramp of $V_{be} = 1.0$ V is applied to the base of the transistor. The duty cycle of the input voltage is 50% with an "ON" cycle time of 50 ps and "OFF" cycle time of 50 ps. For clarity, the rise and fall times in the waveforms in Fig. 5(a) and (b) are shown only up to 60 ps. The ramp up time of the input voltage is 1 ps. The collector voltage is fixed at $V_c = 1.0$ V and the emitter voltage is fixed at $V_e = 0$ V. Fig. 5(b) represents the collector terminal current response to the aforementioned input base voltage. At a subcollector doping of 1.0×10^{20} cm^{-3} and peak triangular Ge mole fraction of 28% the extracted collector current rise times and fall times are 3.1 ps and 0.9 ps. This corresponds to a bit rate of $1 \div (3.1 + 0.9) = 250$ Gbit/sec. Similarly, at the same

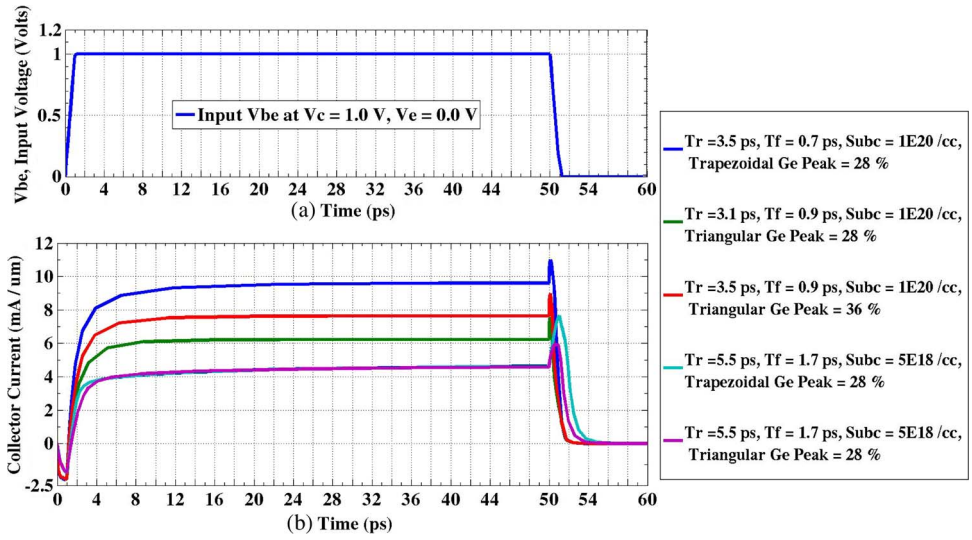

Fig. 5. Transient collector terminal currents from MEDICI simulations. Rise Time (Tr) = (10%−90%) and Fall Time (Tf) = (90%−10%).

subcollector doping of 5.0×10^{18} cm^{-3} and a trapezoidal Ge profile, it is possible to achieve bit rates of 138 Gbit/s. The essence of having the $V_c = 1.0$ V is to reduce excessive minority carrier injection in the collector-base junction, thus ensuring fast turn-off times of ~0.9 ps. For a subcollector doping of 5.0×10^{18} cm^{-3} high-injection conditions onset at a lower voltage of $V_{be} = 0.93$ V and 0.86 V for a triangular and trapezoidal Ge profile of 28%, respectively (see Fig. 4), compared with the subcollector doping of 1.0×10^{20} cm^{-3}. We chose to operate at $V_{be} = 1$ V instead of $V_{be} = 0.93$ V and 0.86 V because a higher voltage leads to higher carrier concentration and better phase modulation efficiency. Additionally, we report here a comparative study of the switching speed with similar phase modulation efficiency. However, operation beyond 1 V reduces the switching speed to below 138 Gbit/s.

For an optical modulator, it is essential to study the transient electron hole distribution along the vertical direction of carrier transport. Fig. 6 shows the transient electron-hole distribution for a subcollector doping of 1.0×10^{20} cm^{-3} and a peak triangular Ge mole fraction of 36%. This case is chosen since the integral Ge content in 28% trapezoidal profile is the same as 36% triangular profile (i.e., fixed film stability). Additionally, extracted rise and fall times of the collector current are 3.5 ps and 0.9 ps, respectively, thus supporting high-speed operation. Fig. 6(a) shows the evolution of the electron and hole concentrations at the center of the cross section (along AA′ of Fig. 1) during the rise time. The rise time of the optical modulator corresponds to the difference in the t_1 (time at 0.9 Q_{max}) and t_2 (time at 0.1 Q_{max},) where Q_{max} is the maximum electron or hole concentration at the center of the cross section (along AA′ of Fig. 1) when the carrier concentration is saturated. The SIC has a lateral width of 90 nm below the SiGe base. Hence, analyzing the 1-D cut at the center will ensure that we consider the rise and fall times of the electron and hole concentrations which account for maximum phase modulation efficiency. However, the speeds of injection-type silicon light modulators are limited by the minority carrier injection time. Hence, we report here the most conservative rise and fall times when we consider the minority carrier electrons in the base with $Q_{max} = 3.0 \times 10^{18}$ cm^{-3}. From Fig. 6(a), $t_1 = 5$ ps, and $t_2 = 1.46$ ps. Hence, the rise time of the modulator is 3.54 ps. Similarly the fall time of the modulator corresponds to the difference in the t_3 (time at 0.9 Q_{max}) and t_4 (time at 0.1 Q_{max},) where Q_{max} is the maximum electron or hole concentration when the carrier concentration is saturated. From Fig. 6(b), $t_3 = 50.2$ ps, and $t_4 = 50.5$ ps. Hence, the fall time of the modulator is 0.3 ps. The reciprocal of the sum of rise and fall times corresponds to a data rate of ~250 Gbit/s.

The base input ramp-up time and ramp-down time of 1 ps is used in the extraction of the transient curves, as shown in Figs. 5(a) and (b) and 6(a) and (b) under the large signal conditions. However,

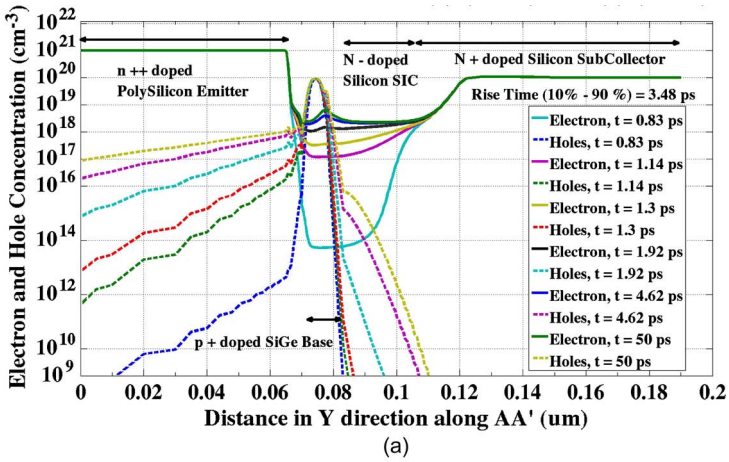

(a)

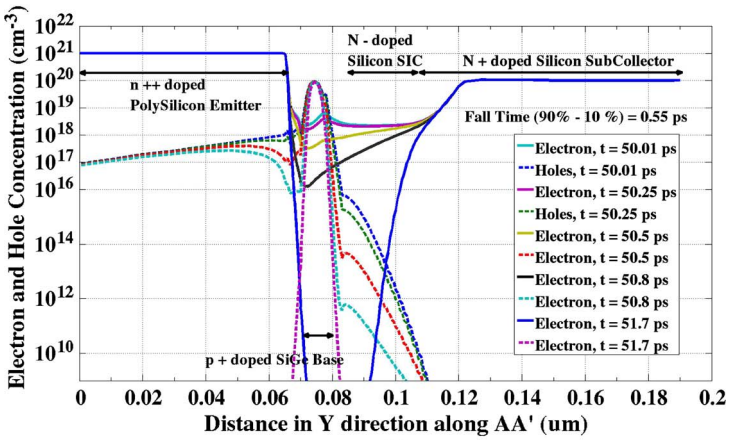

(b)

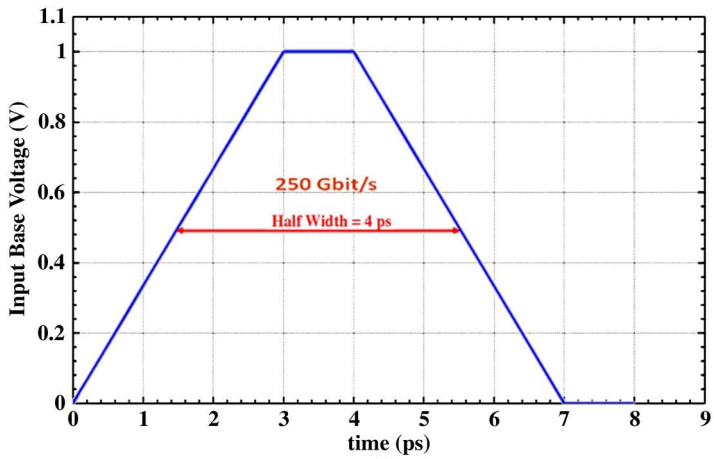

(c)

Fig. 6. Time evolution of free carriers for $V_{be} = 0$ to 1.0 V. (a) Electron and Hole Rise Time = 3.48 ps. (b) Electron and Hole Fall Time = 0.55 ps. (c) Input voltage transient with ramp-up and ramp-down times of 3 ps.

a more reasonable estimate of the switching speed of the SiGe HBT when integrated with a driver is required. Hence, a more practical value of an input base voltage transient of 250 Gbit/s with a ramp-up and ramp-down time of 3 ps is shown in Fig. 6(c). At 3 ps of input ramp-up time and ramp-down time, the collector current overshoots and undershoots are negligible. The switching speed of the

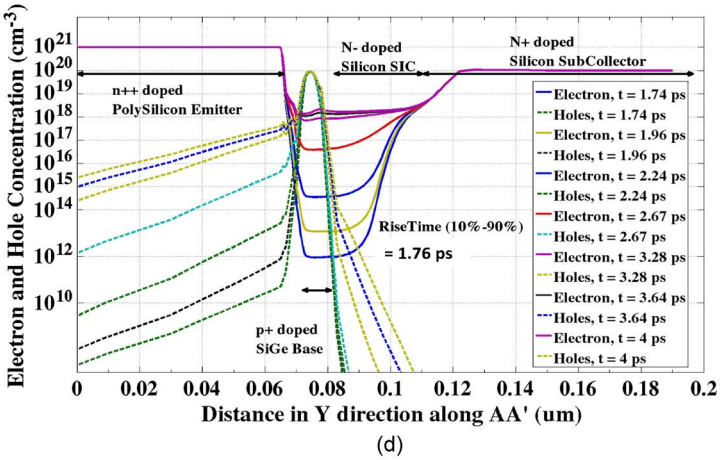

(d)

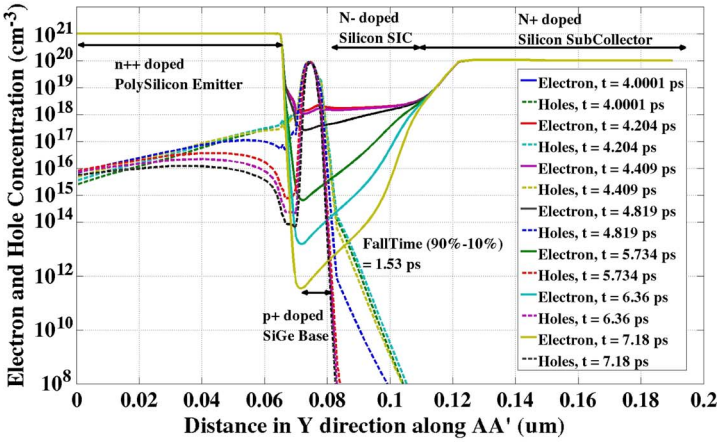

(e)

Fig. 6. (*Continued.*) Time evolution of free carriers for $V_{be} = 0$ to 1.0 V. (d) Electron and Hole Rise Time = 1.76 ps. (e) Electron and Hole Fall Time = 1.53 ps.

carriers under this input bias level is extracted to have a rise time of 1.76 ps and a fall time of 1.53 ps, as shown in Fig. 6(d) and (e). This corresponds to a switching speed of 303 Gbit/s. This concludes our analysis that the switching speed of the modulator at 250 Gbit/s or higher is theoretically possible.

4.1.3. Forward Gummel, Current Gain, and Output Characteristics

To analyze the operation of the E-B junction, the forward Gummel characteristics were extracted from MEDICI by applying a V_{be} sweep from 0 to 1.2 V with $V_{cb} = 0$ V. The extracted plots are illustrated in Fig. 7. The Slotboom BGN model is used to illustrate the impact of high doping effects in the SiGe HBT. According to the Slotboom model, the bandgap of a semiconductor material is given by [8], [14]

$$\Delta E = V_0 \times \left[\ln \frac{N_{\text{total}}}{N0} + \sqrt{\left(\ln \frac{N_{\text{total}}}{N0} \right)^2 + k} \right] \tag{3}$$

where ΔE is the bandgap change due to heavy doping effects, N_{total} is the intrinsic doping level used in the device (see Fig. 2), and k is Boltzmann's constant. The BGN model parameters includes a voltage parameter, V_0, a constant parameter, k, and a concentration parameter, $N0$. The parameter values are chosen to be V_0 of 6.5×10^{-3} eV, $N0$ of 1.3×10^{17} cm^{-3}, and k of 0.5 for Si

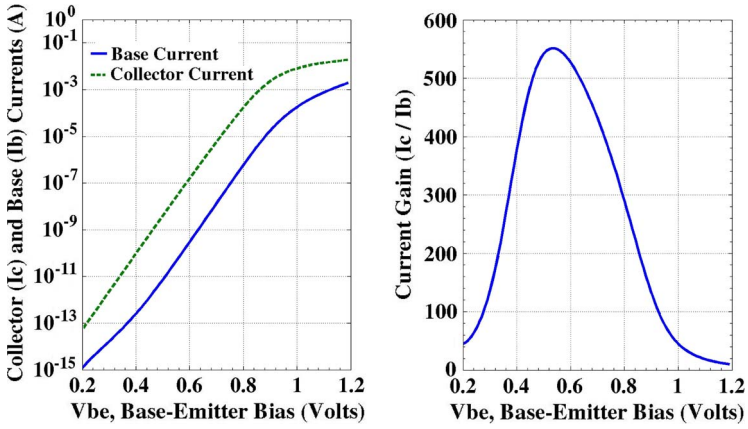

Fig. 7. Forward Gummel characteristics (left) and Current gain (right) of the SiGe HBT.

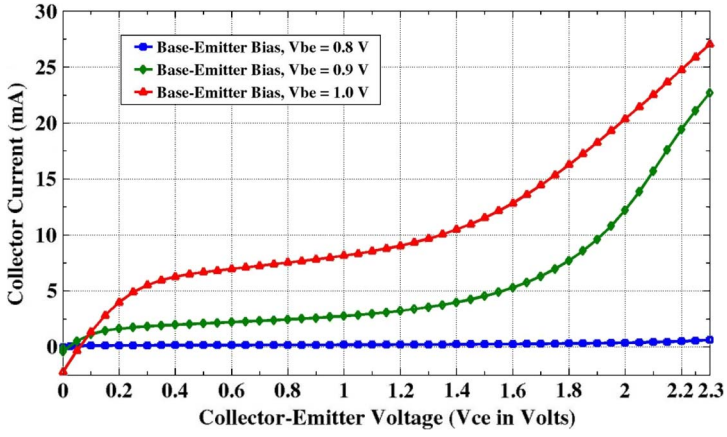

Fig. 8. Output Characteristics of the SiGe HBT.

and SiGe regions. The dominant component of base current at biases lower than 0.4 V is due to recombination effects rather than diffusion of carriers. Hence, the lifetime parameters play a critical role at those bias levels. As the forward bias is increased above 0 V, the base current is dominated by recombination of carriers. At larger forward bias the injection of electrons leads to larger collector current and hence higher current gain, as shown in Fig. 7.

The output characteristics of the SiGe HBT are simulated at a fixed V_{be} of 0.8 V, 0.9 V, and 1.0 V, with V_{ce} from 0 V to 2.3 V, as shown in Fig. 8. The impact ionization model is turned on to simulate possible breakdown conditions. The output characteristics also illustrate the feasibility of the sufficient collector-emitter reverse bias voltage without breaking down the collector base junction. Hence, our assumption that we can operate this device at a collector bias of 1.0 V is reasonable.

4.2. Optical Property Analysis

4.2.1. Sentaurus DC Carrier Densities and Refractive Index Profiles

As discussed in Section 4.1.2, we chose to use $V_{be} = 1.0$ V as the forward bias switching voltage to the base of the modulator. Using a physical model interface (PMI) [9], the dependence of refractive index on carrier densities for each semiconductor region based on Soref's equations is included. Two separate DC solutions are executed: one at a forward-bias voltage of $V_{be} = 1.0$ V, $V_c = 1.0$ V, $V_e = 0.0$ V and the other at an unbiased condition of $V_{be} = 0.0$ V, $V_c = 1.0$ V,

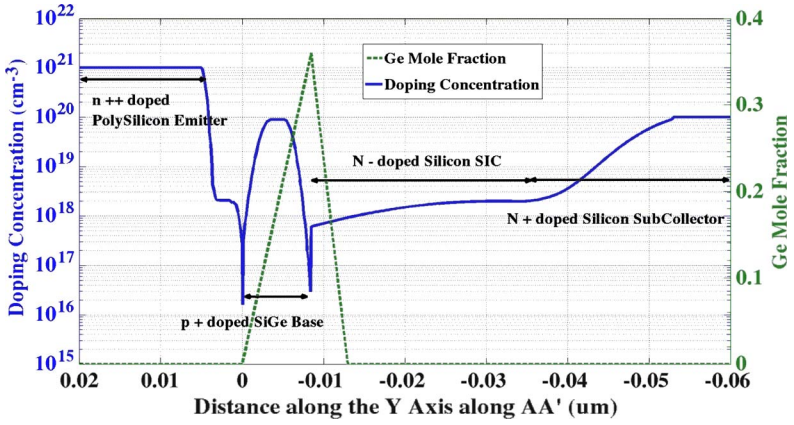

Fig. 9. Doping and Ge mole-fraction in Sentaurus.

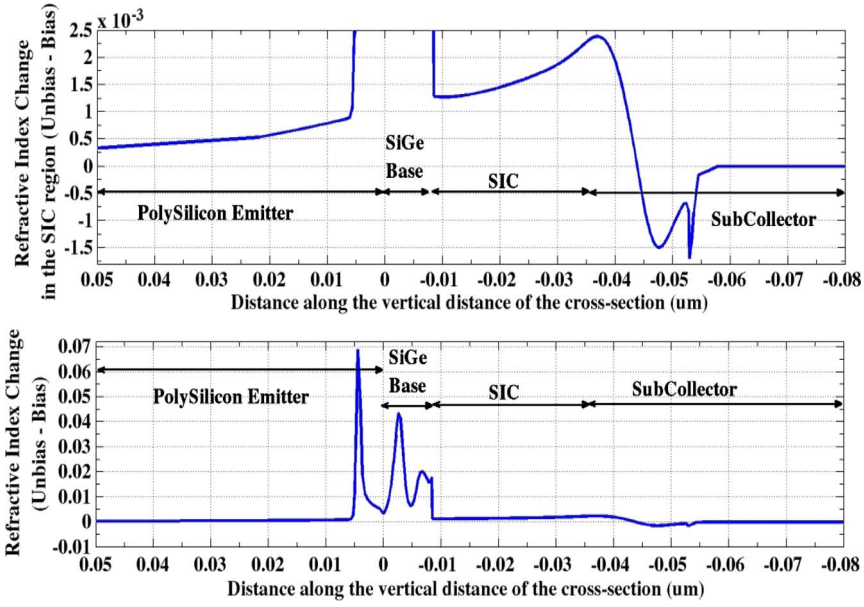

Fig. 10. Refractive Index change at the center of the cross-section of the device along AA′ (bottom) and an expanded view of the refractive index change in the SIC region (top).

$V_e = 0.0$ V. The doping profile and the Ge mole fraction are shown in Fig. 9. The change in the distribution of carrier densities during forward-bias conditions is responsible for the change in the refractive index and, hence, the change of the phase constant of the optical mode in the waveguide section of the device. The resulting change of refractive index distribution between the on and off states is shown in Fig. 10. The waveguide of this device consists of the region between the two shallow trenches in the lateral direction and between the SiGe base and the buried (BOX) layer. The highly doped emitter $(1.0 \times 10^{21}\ \text{cm}^{-3})$ generates a much lower refractive index ($\sim$2.5) compared with Si (3.45). Additionally, the SiGe base is 8.5 nm thick. The change in refractive indices in the base contributes less to the change in propagation constant and the power loss of the optical mode since optical field intensity is lower in the base compared with the SIC. The change of refractive indices in the SIC contributes to the maximum change in the phase and absorption losses of the optical mode. Hence, the switching speed and the length of the modulator are mostly determined by the switching speed and the amount of carriers in the SIC, respectively. From

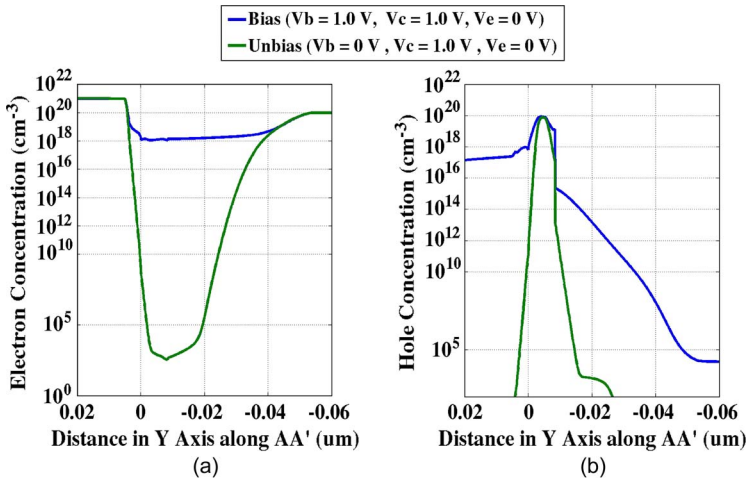

Fig. 11. (a) Electron Density and (b) Hole Density at Unbiased (green) and Biased (red) condition.

Fig. 11(a) and (b), it is clear that the electrons in SIC undergo more change during the switching from unbiased to biased condition. This also translates into faster switching speed. Too much injection of holes in the SIC at very high V_{be} bias will increase the change in phase constant but, at the same time, reduce the switching speed of the modulator.

4.2.2. Transmission Characteristics of L_π, Attenuation, and Extinction Ratio

The propagation constant and the effective indices of the SiGe HBT waveguide are computed at different bias conditions. Since the transverse magnetic (TM) mode resulted in better interaction with free carrier plasma and thus smaller L_π, the following discussion is based only of the TM mode. The turn-on switch is controlled by the V_{be} bias, varying between 0 V and 1.0 V. In this work, we analyze in detail how the propagation constant changes along the length of the modulator. Because the variation of carrier concentration takes place near the base and the SIC, it is favorable to push the optical mode closer to the SIC in order to obtain the maximum index modulation over the optical field.

A Gaussian beam of wavelength $\lambda = 1.55$ μm and half width of 0.6×0.6 μm is launched at $Z = 0$ μm. The waveguide region in this device is that of the rib waveguide. As we have mentioned in Section 2, the device structure is constructed for optimal electrical and optical operation. To achieve the single mode condition, we must satisfy [25]

$$\frac{W}{H} \leq 0.3 + \frac{r}{\sqrt{(1 - r^2)}}, \qquad \text{for } 0.5 \leq r \leq 1.0 \tag{4}$$

where, W, H, and r are defined in Fig. 12(a).

Here, $W = 0.6$ μm, $H = 0.615$ μm, $h = 0.35$ μm, $r = 0.5691$, and $W/H = 0.975$. The right-hand side of (4) is 0.9921. The bidirectional feature of BPM is turned on. The optical tensor mesh output is chosen with fine grid spacing to ensure accurate results. A grid resolution of approximately 1.3 nm is chosen in the X and Y directions for nanoscale feature sizes of the base and SIC region. The Z direction meshing is carefully chosen to 4.6 nm to account for accurate prediction of optical phase and loss. The output optical mode is shown in Fig. 12(b). The stable mode profile at the output end is confined between the two lateral shallow trench oxides and vertically by the BOX layer at the bottom and highly doped emitter and spacer oxides at the top.

A Perl script is executed in order to extract the propagation constant from the real and imaginary output optical fields at each point from $Z = 0$ μm to $Z = 10$ μm and different X, Y coordinates

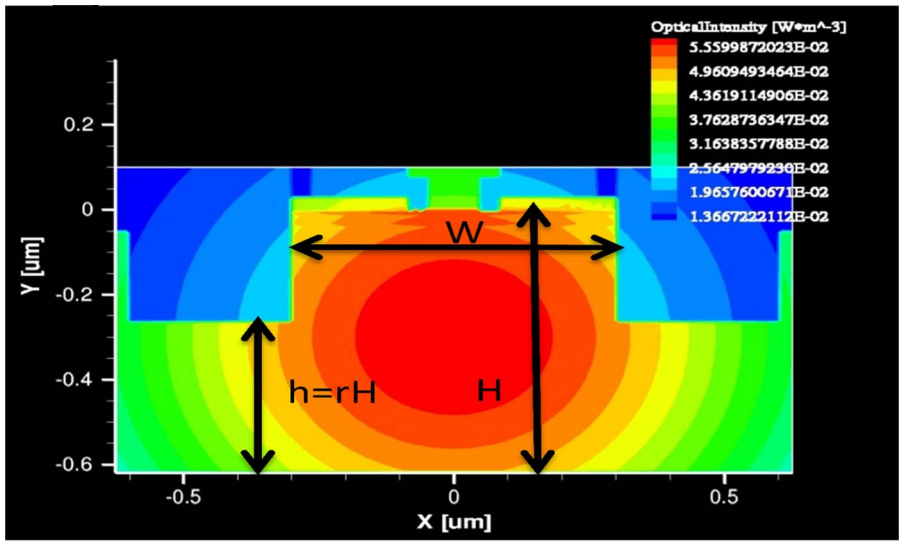

(a)

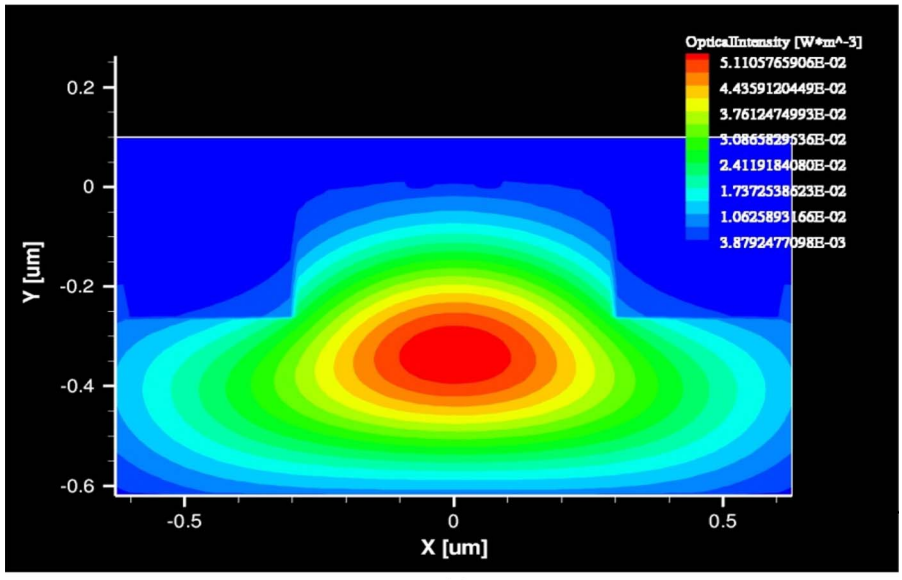

(b)

Fig. 12. (a) Input optical mode profile at $Z = 0$ μm. (b) Output optical mode at $Z = 10$ μm.

where the peak optical field resides. The complex propagation constant (γ) consists of an attenuation constant (α) and phase constant (β). We know from [21]

$$E(x, y) = E_0(x, y) * \exp(-\gamma d) \tag{5}$$

where $Y = \alpha + j\beta$ and $E(x, y)$ and $E_0(x, y)$ are propagation constant and electric fields, respectively, at a particular point in Z.

The transmission coefficient

$$T = \frac{E(x, y)}{E0(x, y)} = \exp(-\gamma d). \tag{6}$$

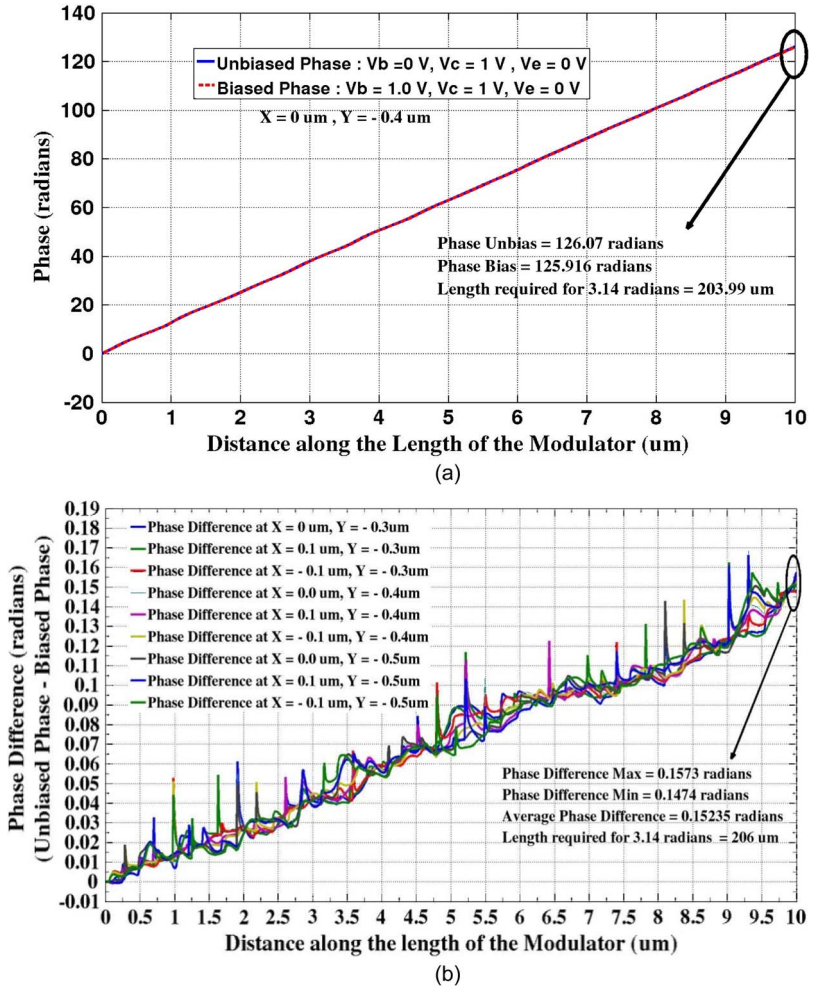

Fig. 13. (a) Phase versus length of the modulator (b) Phase difference versus length of the modulator.

Then

$$\beta = -\left(\frac{2\pi d + \phi}{d}\right) \tag{7}$$

where $\phi = \arctan\{\text{Imag(Optical Field)}/\text{Real(Optical Field)}\}$, and d is the distance along the length of the Modulator.

The phase ϕ is extracted for the center of the beam at $X = 0$ μm, $Y = -0.4$ μm along different points in the length of the modulator. Fig. 13(a) illustrates the phase of the optical mode along the length of the modulator. At $Z = 10$ μm, the phase at unbiased condition, $p_1 = 126.07$ rad, and the phase in biased condition is $p_2 = 125.916$ rad. The corresponding propagation constants are $\beta_1 = 12.607$ and $\beta_2 = 12.5916$. The wavelength of light (λ) used is 1.55 μm.

The corresponding effective refractive index during unbiased condition: $n\text{eff}_{\text{unbias}} = \beta_1/(2\pi/\lambda) = 3.11002287$, while the corresponding effective refractive index during biased condition: $n\text{eff}_{\text{bias}} = \beta_2/(2\pi/\lambda) = 3.106223841$. The change in effective refractive index $\Delta n_{\text{eff}} = n\text{eff}_{\text{unbias}} - n\text{eff}_{\text{bias}} = 3.799029 * 10^{-3}$, and the length required to obtain the π phase shift $= \lambda/(2 * (\Delta n_{\text{eff}})) \sim 203.99$ μm ~ 204 μm.

Fig. 13(b) also shows the phase difference across different points in the peak optical field output. In this plot we take 1-D cutlines from the input end of the optical mode to the output end of the

optical mode at different points of X and Y. This is reported to ensure that the fundamental optical mode, which moves up, down, and laterally as it propagates along the length, undergoes similar phase shifts between the biased arm and the unbiased arm across various points in X and Y dimensions. The average L_π predicted using this technique across different X–Y points is 206 μm. This is fairly close to the 204 μm (L_π, when the cutline is taken at the center of the beam) but not exactly the same because of using 1-D cutline across length even though the center of the beam not exactly at the center as it propagates. This difference in L_π and the reason for the small bumps and overshoots of Fig. 13(b) is attributed to the assumption of using 1-D cutline along the length for extracting the phase. In order compute the optical loss due to the propagating mode, the optical Intensity is monitored from the launch to the output end. Fig. 12(a) and (b) shows the optical mode intensities at the input I_0 ($Z = 0$ μm) and at the output end I_{out} ($Z = 10$ μm). $I_0 = 5.55998 \times 10^{-2}$ W/m^3 and $I_{\text{out}} = 5.11053 \times 10^{-2}$ W/m^3. Hence, the propagation loss $= 10 \times \log(I_{\text{out}}/I_0) = 0.0366$ dB/μm. Thus, for the total active length of the modulator of 204 μm, the optical power loss $= 0.0366 * 204 = 7.46$ dB.

To evaluate how efficiently the light signal's intensity is modulated, the extinction ratio can be examined as an figure-of-merit and is defined as the ratio of the output intensity variations that represent logic level "1" (I_H) and "0" (I_L). The expression for extinction ratio in decibels can be written as $10 \times \log(I_H/I_L)$. In our proposed MZI structure, one arm is kept unbiased as a reference, while the other one is switched to produce the intensity difference. Considering the significant loss in the SiGe HBT EO modulator, both arms are equipped with the same SiGe HBT structure. In this way, the output intensity from each arm is comparable, and the extinction ratio is greatly improved. However, it is worth noting that despite the high extinction ratio value, a photodetector with high sensitivity is necessary because the absolute level of intensity is low as a result of the high loss. Denote the intensity at the output of the reference arm as I_1 and that on the modulation arm as I_2 and I_2' when the modulator is OFF and ON, respectively. Considering that the phase difference varies from 0 to ϕ when the output intensity changes from high to low, I_H and I_L is obtained as $I_H = I_1 + I_2 = 2I_1$ and $I_L = I_1 - I_2'$. The extinction ratio for the MZI structure is thus $10 \times \log[2I_1/(I_1 - I_2')]$. Based on the mode computation results reported above, the extinction ratio is calculated to be 13.2 dB when the EO modulator switches between 0 V and 1.0 V.

4.3. Dynamic Power Consumption

The dynamic power of the device of 204 μm length is evaluated by

$$\text{Energy/bit} = 0.5 \times \int_0^{t_s} (I_c(t) V_{\text{ce}}(t) + I_B(t) V_{\text{be}}(t))\, dt \tag{8}$$

where I_c is the collector current, and I_b is the base current, as shown in Fig. 14, V_{ce} is the collector-emitter voltage, and V_{be} is the base-emitter voltage. The factor 0.5 in (8) accounts for the fact that the "ON" state appears with 50% possibility in a long random Non-Return-to-Zero (NRZ) pulse train. The minimum pulse width (i.e., the maximum data rate) is limited by the response time. According to our transient analysis, the smallest t_s is 4 ps, and the inverse of t_s gives a maximum bit rate of 250 Gbit/s. Based on the above assumptions, the dynamic energy consumption is 2.01 pJ/bit at V_{be} of 1.0 V, which is lower than 3.6 pJ/bit at 80 Gbit/s [7] but higher than that of 400 fJ/bit [22]. The proposed device in this study when switched at a slower speed of 80 Gbit/s will operate at a much lower collector and base current levels and, hence, comparable energy per bit. For operating this device at a slower speed the subcollector doping can be reduced from 1.0×10^{20} cm^{-3} to 5.0×10^{18} cm^{-3} as shown in Fig. 4. This results in reduced collector current levels, as shown in Fig. 5(b), and, hence, is comparable with or lower energy/bit for the same modulation efficiency.

The input voltage swing can be reduced to 0.5 V by operating the modulator with a base swing voltage from 0.5 V to 1.0 V. This makes implementation of driver circuits simpler. To enhance this basic SiGe HBT modulation it will be necessary to devise a low Q resonator that is compatible with the SiGe HBT electrical structure and which will still permit a small amount of reuse of the plasma.

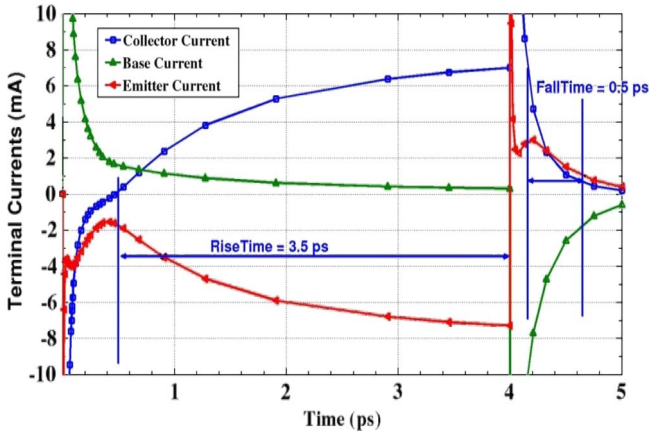

Fig. 14. One bit transient Terminal Currents for Input base ramp of 1 V with ramp time = 1 fs during "Rise Time" and fixed $V_c = 1$ V during "Rise Time" and "Fall Time."

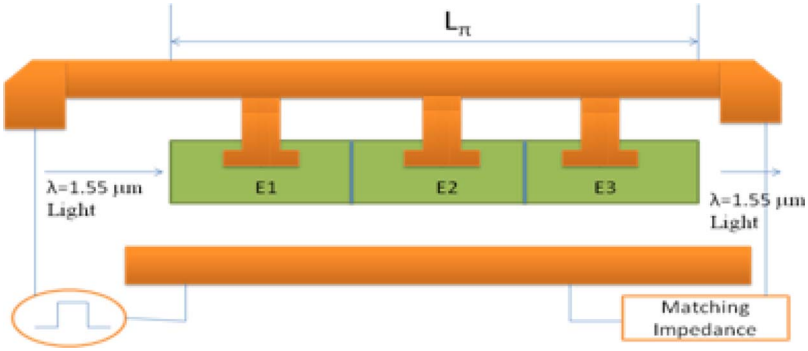

Fig. 15. Schematic of the emitter segmented modulator driven by TWE configuration. E1, E2, and E3 in the sketch denote the emitter segment 1, 2, and 3, respectively.

Based upon prior work, an assumed Q of only 10–30 could considerably shorten the device and lower its power consumption [23], [24], [26].

Parasitic resistances and capacitances introduced by the electrical contact pads required for longer length of the device will degrade the operational bandwidth. One way to overcome this bandwidth limitation is to break the long phase shifter into smaller segments and drive every segment with the same signal delayed by appropriate skew. This configuration can be interpreted as a TWE, as shown in Fig. 15. The fundamental idea underlying the TWE in contrast to lumped electrodes is the fact that the distributed capacitance does not limit the modulator speed [28]. Proper design will enable identical propagation speed of the optical and the modulating electrical signal, permitting the phase modulation to accumulate monotonically irrespective of frequency. Another possible configuration is to use the SiGe HBT as an amplitude modulator.

5. Comments on the Path Towards Experimental Verification

This work is based upon calibrated technology computer-aided design (TCAD) simulations and represents an important first step to confirm the theoretical practicality of using SiGe HBTs to realize ultrahigh-speed SiGe-based EO modulators. Clearly, however, the path to an experimental proof-of-concept is highly desirable. While that result is not on the immediate horizon, several general comments are worth making. First, the structure and vertical profiles of the SiGe HBT needed to support these types of speeds in the EO domain are aggressive (e.g., 600 GHz peak f_T) but not impractical. It is increasingly well accepted that performance levels approaching terahertz will be

experimentally achievable in SiGe, and in fact, f_{max} above 600 GHz has already been demonstrated at cryogenic temperatures in a conservative 130-nm SiGe HBT [27]. Multiple groups are presently pursuing 500-GHz SiGe HBTs at 300 K, and this appears to be a very reasonable performance target while maintaining the virtues of fully silicon-compatible manufacturing. This SiGe HBT for the EO modulator requires 90-nm lithography, but this is fairly routine (very conservative by CMOS standards), and existing fourth-generation SiGe platforms already use 90 nm today. The SiGe HBT needed for the EO modulator also requires SOI underneath the transistor for optical confinement, but again, there is precedence for doing this. Best-of-breed SiGe analog platforms have already made use of thick-film SOI for improved isolation for several years now. While adding SOI does indeed add process complexity, it has been repeatedly demonstrated as a viable path in SiGe. Finally, this SiGe HBT for the EO modulator must interface seamlessly with the requisite on-die optical wave guiding. This will present several complexities in fabrication but is viewed as only a problem requiring development effort. Taken together, while there are clearly significant challenges ahead to reduce the concept presented in this paper to experimental practice, they are not viewed as insurmountable, and the potential of an on-die, all-silicon-based high-speed SiGe EO modulator with supporting on-die electronics remains exceptionally appealing.

6. Summary

This paper reports the highly scaled device structure design as well as the electrical and optical property analysis of a 240–250 Gbit/s SiGe HBT EO modulator. Positive ramp voltages of 1.0 V are applied at the base, and the free carrier dispersion effect is utilized to achieve an EO modulation. An L_π of 204 μm is modeled with rise and fall times of 3.48 ps and 0.55 ps. With these excellent results, we report the feasibility via modeling of a 240–250 Gbit/s SiGe HBT EO modulator attractive for high-speed silicon photonic integrated circuits. Further improvements in L_π can be made by slow light interaction with the carrier plasma without degrading the operation speed. An added advantage in opting for this type of device implementation is that it is compatible voltage with the implementation of on-die driver circuits using the SiGe BiCMOS technology platform.

Acknowledgment

The authors wish to express their deepest thanks to Dr. H. D. Dardy for providing inspiration for this research, as well as his enthusiastic support during his lifetime.

References

[1] W. M. Green, M. J. Rooks, L. Sekaric, and Y. A. Vlasov, "Ultra-compact, low RF power, 10 Gb/s silicon Mach–Zehnder modulator," *Opt. Exp.*, vol. 15, no. 25, pp. 17 106–17 113, Dec. 2007.
[2] A. Liu, L. Liao, D. Rubin, H. Nguyen, B. Ciftcioglu, Y. Chetrit, N. Izhaky, and M. Paniccia, "High-speed optical modulation based on carrier depletion in a silicon waveguide," *Opt. Exp.*, vol. 15, no. 2, pp. 660–668, Jan. 2007.
[3] F. Gardes, G. Reed, N. Emerson, and C. Png, "A sub-micron depletion-type photonic modulator in Silicon on Insulator," *Opt. Exp.*, vol. 13, no. 22, pp. 8845–8854, Oct. 31, 2005.
[4] Y. Tang, H.-W. Chen, S. Jain, J. D. Peters, U. Westergren, and J. E. Bowers, "50 Gb/s hybrid silicon traveling-wave electroabsorption modulator," *Opt. Exp.*, vol. 19, no. 7, pp. 5811–5816, Mar. 2011.
[5] J. C. Rosenberg, W. M. Green, S. Assefa, T. Barwicz, M. Yang, S. M. Shank, and Y. A. Vlasov, "Low-power 30 Gbps silicon microring modulator," in *CLEO—Laser Applications Photonic Applications, OSA Tech. Dig.*, (CD), Baltimore, MD, 2011, Paper PDPB9.
[6] R. D. Lareau, L. Friedman, and R. A. Soref, "Waveguided electro-optical intensity modulation in a Si/Ge$_x$Si$_{1-x}$/Si heterojunction bipolar transistor," *Electron. Lett.*, vol. 26, no. 20, pp. 1653–1655, Sep. 27, 1990.
[7] T. Guha Neogi, S. Deng, J. Novak, J.-R. Guo, R. Clarke, M. R LeRoy, J. F. McDonald, and Z. R. Huang, "Modeling and analysis of an 80-Gbit/s SiGe HBT electrooptic modulator," *IEEE Photon. J.*, vol. 3, no. 1, pp. 42–56, Feb. 2011.
[8] Synopsys, *Taurus Medici User Guide*, Mar. 2007, Ver. Z-2007.03.
[9] Synopsys, *Sentaurus Device User Guide*, Dec. 2010, Ver. Z-2010.12.
[10] Y. Shi and G. Niu, "2-D analysis of device parasitics for 800/1000 GHzf_T/f_{max} SiGe HBT," in *Proc. Bipolar/BiCMOS Circuits Technol. Meeting*, Oct. 9–11, 2005, pp. 252–255.
[11] L. Liao, D. Samara-Rubio, A. Liu, D. Rubin, U. D. Keil, T. Franck, D. Hodge, and M. Paniccia, "High speed metal-oxide-semiconductor capacitor-based silicon optical modulators," *Jpn. J. Appl. Phys.*, vol. 45, pp. 6603–6608, 2006.
[12] Y. Shi, "Design and optimization of nano-scaled silicon-germanium heterojunction bipolar transistors," Ph.D. dissertation, Auburn Univ., Auburn, AL, 2005.

[13] J. W. Slotboom, "The pn-product in Silicon," *Solid State Electron.*, vol. 20, no. 4, pp. 279–283, Apr. 1977.
[14] D. B. M. Klaassen, J. W. Slotboom, and H. C. de Graaff, "Unified apparent bandgap narrowing in n- and p-type Silicon," *Solid State Electron.*, vol. 35, no. 2, pp. 125–129, Feb. 1992.
[15] Y. Shi, G. Niu, J. D. Cressler, and D. L. Harame, "On the consistent modeling of band-gap narrowing for accurate device-level simulation of scaled SiGe HBTs," *IEEE Trans. Electron Devices*, vol. 50, no. 5, pp. 1370–1377, May 2003.
[16] A. Cutolo, M. Iodice, P. Spirito, and L. Zeni, "Silicon electro-optic modulator based on a three terminal device integrated in a low-loss single-mode SOI waveguide," *J. Lightw. Technol.*, vol. 15, no. 3, pp. 505–518, Mar. 1997.
[17] C. T. Shih, Z. W. Zeng, and S. Chao, "Design and analysis of metal-oxide-semiconductor—Capacitor microring optical modulator with solid-phase-crystallization poly-silicon gate," *J. Lightw. Technol.*, vol. 27, no. 17, pp. 3861–3873, Sep. 1, 2009.
[18] R. A. Soref and B. R. Bennett, "Electrooptical effects in silicon," *IEEE J. Quantum Electron.*, vol. QE-23, no. 1, pp. 123–129, Jan. 1987.
[19] S. Manipatruni, Q. Xu, B. Schmidt, J. Shakya, and M. Lipson, "High speed carrier injection 18 Gb/s silicon micro-ring electro-optic modulator," in *Proc. 20th Annu. Meeting IEEE LEOS*, Oct. 21–25, 2007, pp. 537–538.
[20] L. Liao, D. Lim, A. Agarwal, X. Duan, K. Lee, and L. Kimerling, "Optical transmission losses in polycrystalline silicon strip waveguides: Effects of waveguide dimensions, thermal treatment, hydrogen passivation, and wavelength," *J. Electron. Mater.*, vol. 29, no. 12, pp. 1380–1386, Dec. 2000.
[21] Z. Abbas, R. D. Pollard, and R. W. Kelsall, "Determination of the dielectric constant of materials from effective refractive index measurements," *IEEE Trans. Instrum. Meas.*, vol. 47, no. 1, pp. 148–152, Feb. 1998.
[22] X. Zheng, J. Lexau, Y. Luo, H. Thacker, T. Pinguet, A. Mekis, G. Li, J. Shi, P. Amberg, N. Pinckney, K. Raj, R. Ho, J. E. Cunningham, and A. V. Krishnamoorthy, "Ultra-low-energy all-CMOS modulator integrated with driver," *Opt. Exp.*, vol. 18, no. 3, pp. 3059–3070, Feb. 2010.
[23] Y. Jiang, W. Jiang, L. Gu, X. Chen, and R. T. Chen, "80-micron interaction length silicon photonic crystal waveguide modulator," *Appl. Phys. Lett.*, vol. 87, no. 22, p. 221 105, Nov. 2005.
[24] J. F. McDonald, H. D. Dardy, and J. R. Guo, *Direct Light Modulation in Silicon with a Graded Base SiGe HBT Through its Carrier Plasma -using 3D Wafer Stacking Techniques to Incorporate a Photonic Slow Wave Device into the Drude Effect Phase Shifter and Associated Photonic Waveguide,* NRL disclosure #97873, Mar. 2005, provisional patent application 61/310754- filed Mar. 5, 2010.
[25] R. A. Soref, J. Schmidtchen, and K. Petermann, "Large single-mode rib waveguides in GeSi-Si and Si onSiO_2," *IEEE J. Quantum Elect.*, vol. 27, no. 8, pp. 1971–1974, Aug. 1991.
[26] J. F. McDonald, R. P. Kraft, J. R. Guo, P. Belemjian, O. Erdogan, P. Jacobs, A. Zia, Y. Yim, M. Chu, J. W. Kim, J. Diao, and J.-Q. Lu, "A slow wave photonic crystal enhancement of SiGe HBT drude-effect light modulators for intra-chip optical interconnections using 3D wafer bonding techniques," in *Proc. 23rd Int. VMIC06*, Freemont, CA, Sep. 26–28, 2006, pp. 243–248.
[27] J. Yuan, J. D. Cressler, R. Krithivasan, T. Thrivikraman, M. H. Khater, D. C. Ahlgren, A. J. Joseph, and J.-S. Rieh, "On the performance limits of cryogenically-operated SiGe HBTs and its relation to scaling for TeraHertz speeds," *IEEE Trans. Electron Devices*, vol. 56, no. 5, pp. 1007–1019, May 2009.
[28] H. Chen, "Development of an 80 Gbit/s InP-based Mach–Zehnder modulator," Ph.D. dissertation, Berlin Univ. Technol., Berlin, Germany, 2007.